The Sun at millimeter wavelengths

I. Introduction to ALMA Band 3 observations[*]

Sven Wedemeyer[1,2], Mikolaj Szydlarski[1,2], Shahin Jafarzadeh[1,2], Henrik Eklund[1,2], Juan Camilo Guevara Gomez[1,2], Tim Bastian[3], Bernhard Fleck[4], Jaime de la Cruz Rodriguez[5], Andrew Rodger[6], and Mats Carlsson[1,2]

[1] Rosseland Centre for Solar Physics, University of Oslo, Postboks 1029 Blindern, 0315 Oslo, Norway
  e-mail: sven.wedemeyer@astro.uio.no
[2] Institute of Theoretical Astrophysics, University of Oslo, Postboks 1029 Blindern, 0315 Oslo, Norway
[3] National Radio Astronomy Observatory (NRAO), 520 Edgemont Road, Charlottesville, VA 22903, USA
[4] ESA Science and Operations Department, c/o NASA Goddard Space Flight Center, Greenbelt, MD 20771, USA
[5] Institute for Solar Physics, Dept. of Astronomy, Stockholm University, Albanova University Center, 10691 Stockholm, Sweden
[6] SUPA, School of Physics and Astronomy, University of Glasgow, Glasgow G12 8QQ, UK

ABSTRACT

Context. The Atacama Large Millimeter/submillimeter Array (ALMA) started regular observations of the Sun in 2016, first offering receiver Band 3 at wavelengths near 3 mm (100 GHz) and Band 6 at wavelengths around 1.25 mm (239 GHz).
Aims. Here we present an initial study of one of the first ALMA Band 3 observations of the Sun. Our aim is to characterise the diagnostic potential of brightness temperatures measured with ALMA on the Sun.
Methods. The observation covers a duration of 48 min at a cadence of 2 s targeting a quiet Sun region at disc-centre. Corresponding time series of brightness temperature maps are constructed with the first version of the Solar ALMA Pipeline and compared to simultaneous observations with the Solar Dynamics Observatory (SDO).
Results. The angular resolution of the observations is set by the synthesised beam, an elliptical Gaussian that is approximately $1.4'' \times 2.1''$ in size. The ALMA maps exhibit network patches, internetwork regions, and elongated thin features that are connected to large-scale magnetic loops, as confirmed by a comparison with SDO maps. The ALMA Band 3 maps correlate best with the SDO/AIA 171 Å, 131 Å, and 304 Å channels in that they exhibit network features and, although very weak in the ALMA maps, imprints of large-scale loops. A group of compact magnetic loops is very clearly visible in ALMA Band 3. The brightness temperatures in the loop tops reach values of about 8000−9000 K and in extreme moments up to 10 000 K.
Conclusions. ALMA Band 3 interferometric observations from early observing cycles already reveal temperature differences in the solar chromosphere. The weak imprint of magnetic loops and the correlation with the 171, 131, and 304 SDO channels suggests, however, that the radiation mapped in ALMA Band 3 might have contributions from a wider range of atmospheric heights than previously assumed, but the exact formation height of Band 3 needs to be investigated in more detail. The absolute brightness temperature scale as set by total power measurements remains less certain and must be improved in the future. Despite these complications and the limited angular resolution, ALMA Band 3 observations have a large potential for quantitative studies of the small-scale structure and dynamics of the solar chromosphere.

Key words. Sun: chromosphere – Sun: radio radiation – Sun: atmosphere

1. Introduction

The Atacama Large Millimeter/submillimeter Array (ALMA) provides new diagnostic possibilities to probe the chromosphere of the Sun at high spatial, temporal, and spectral resolution (see Bastian 2002; Wedemeyer 2016; Wedemeyer et al. 2016; Loukitcheva et al. 2017; Bastian et al. 2018, and references therein). In principle, observing at millimetre wavelengths has the advantage that the radiation is formed under conditions of local thermodynamic equilibrium (LTE), and therefore provides a more direct measure of local gas temperatures in the chromosphere than other commonly used diagnostics at shorter wavelengths, such as optical and UV wavelengths, that are not in LTE. The comparatively long millimetre and submillimetre wavelengths have historically had the disadvantage of a correspond-

ingly lower angular resolution, relying largely on single-dish observations (e.g., Bastian et al. 1993; Lindsey et al. 1995, and references therein). Interferometric techniques, using an array of antennas, offer the means of observing the Sun with high angular resolution. These were explored in the 1990s (e.g., Kundu et al. 1993) and 2000s (White et al. 2006) using small arrays. ALMA is the largest and most ambitious array ever built to observe celestial phenomena at millimetre and submillimetre wavelengths, including the Sun. ALMA offers the potential of unlocking this new diagnostic tool for high-resolution studies of the solar chromosphere. An overview of potential science cases with ALMA is given by Wedemeyer et al. (2016), whereas Cycle 4 capabilities are described by White et al. (2017) and Shimojo et al. (2017a). While the first regular ALMA observations of the Sun were only offered in Cycle 4 with a first solar campaign in December 2016, earlier observations from Commissioning and Science Verification (CSV) campaigns have been made publicly

---

[*] Movies are available at https://www.aanda.org

available. Both regular and CSV data are already used in publications: Alissandrakis et al. (2017), Bastian et al. (2017), Shimojo et al. (2017b), Brajša et al. (2018), Nindos et al. (2018), Yokoyama et al. (2018), Jafarzadeh et al. (2019), Loukitcheva et al. (2019), Molnar et al. (2019), Rodger et al. (2019), Selhorst et al. (2019), Patsourakos et al. (2020), da Silva Santos et al. (2020).

Interferometric observations of a dynamic source like the Sun and the reliable reconstruction of corresponding image series are challenging tasks. As a next step, in order to further develop and characterise ALMA's diagnostic capabilities, the available observations have to be thoroughly studied and compared to other diagnostics. Here we present and analyse observations with ALMA Band 3 at wavelengths around 3 mm from December 2016 (Cycle 4), which were among the first regular observations of the Sun with ALMA. The aim of the results presented here is to illustrate the potential, limitations, and challenges of studying the small-scale structure and dynamics of the solar atmosphere with ALMA Band 3. The technical details of the observations are described in Sect. 2 and the results of the data analysis in Sect. 3. Discussion and conclusions are provided in Sects. 4 and 5, respectively.

2. Observations

2.1. Solar observation in Band 3

The Band 3 observations discussed in this article were carried out on December 22, 2016, from 14:22 UT to 15:07 UT. ALMA observations of the Sun currently comprise both interferometric observations of a specific target and full-disc maps made with ALMA total power (TP) antennas. For the interferometric observations an array in configuration C40-3 was used, which included a total of 52 antennas from the 12 m Array in addition to the 10 fixed 7 m antennas of the Atacama Compact Array. The resulting array has baselines ranging from 9.1 m to 492.0 m resulting in a nominal angular resolution of 1.56″ and a maximum recoverable scale (MRS) of 68″. In addition to the interferometric observations, ALMA has up to four specially designed total power (TP) antennas that can perform rapid scans of the whole disc of the Sun (White et al. 2017). For the observations analysed here, three TP antennas were available for fast-scan mapping. The column of precipitable water vapour (PWV) in the Earth's atmosphere during the observation was 1.60 mm.

Because of an operational glitch, the interferometric array did not point at and track the intended target region, but instead re-centred on $[x, y] = [0″, 0″]$ in helioprojective coordinates repeatedly during the observation. As a result, the observed disc-centre quiet Sun region is slowly drifting through the ALMA field of view (FOV) because the telescope pointing did not track solar rotation (see Sect. 2.2). The Band 3 observing sequence consists of four scans with a duration of ∼10 min each. These scans are separated by calibration breaks of ∼2.4 min. The observations were carried out with a cadence of 2 s, the highest possible in Cycle 4.

In Cycle 4, ALMA Band 3 was set up for solar observations in four spectral windows (hereafter referred to as sub-bands) around a central frequency of 100 GHz. These sub-bands, which we refer to as sub-bands 1–4 (SB1–SB4) with increasing frequency, are centred on 93 GHz (SB1), 95 GHz (SB2), 105 GHz (SB3), and 107 GHz (SB4), corresponding to wavelengths of 3.224 mm, 3.156 mm, 2.855 mm, and 2.802 mm. Each sub-band has a total bandwidth of 2 GHz (with the central 1.875 GHz

being retained), which results in two pairs of neighbouring sub-bands (SB1–SB2 and SB3–SB4) with a central gap.

The three available TP maps were completed at 14:23 UT, 14:36 UT, and 14:49 UT. A complete scan in Band 3 took between 12.6 min and 12.9 min, including calibration. The net time for scanning the solar disc in a double-circle pattern is 5 min. The TP maps thus cover most of the interferometric observation and can be used to combine the interferometric and TP data, which results in absolute brightness temperatures. The TP map for SB4 for the first scan (from 14:11 UT to 14:23 UT) is shown in Fig. 1a; see Appendix A.4 for background information regarding the TP observations.

2.2. Interferometric data processing

Approach for the Band 3 data set. The calibrated ALMA data were downloaded from the ALMA Archive and further processed with the Solar ALMA Pipeline (SoAP, Szydlarski et al., in prep.[1]) based on the Common Astronomy Software Applications (CASA[2]) package. We note that solar observing is currently still a non-standard mode. Solar data are therefore not processed with the official ALMA pipeline. Instead, SoAP is used for this publication (see Appendix A.1 for more information on interferometric image reconstruction).

Unique to the data from December 2016 are the complications arising from the erroneous pointing and tracking, which resulted in the instrument phase tracking centre repeatedly being re-pointed to the apparent centre of the solar disc, resulting in a slow drift of the FOV with intermediate jumps. It was therefore necessary to correct for the effect of the Sun's rotation during the course of the observation. To do so, a time series of Band 3 images at 2 s cadence was constructed. The image processing required for each snapshot image includes several important steps. First, the ALMA PSF (the "dirty beam") was deconvolved from the image data (the "dirty map") through application of the multi-scale (multi-frequency) CLEAN algorithm (Rau & Cornwell 2011) as implemented in CASA. Here all interferometric information from the four sub-bands is used to produce one continuum image (the "full-band map") for each time step (see also Appendix A.1). Second, the image data were corrected for the effect of the primary beam (see Sect. 2.3). Third, the interferometric data were combined with the TP map (in a process known as feathering) in order to add a DC brightness offset, and thus the absolute brightness temperature scale corresponding to zero-spacing information to the reconstruction (Sect. 2.5). Finally, the ALMA Band 3 maps were co-aligned with observational data from other observatories (Sect. 2.6). The apparent drift of snapshot images in time due to solar rotation was then corrected by cross-correlating consecutive 2 s images with a reference image, where the first frame in the times series was taken as the reference. The resulting time sequence represents true snapshot imaging at 2 s cadence with no temporal averaging. It should be noted that self-calibration for a short time window is the recommended approach, but that self-calibration resulted in too aggressive corrections and loss of information on small spatial scales for the December 2016 data, which suffered from pointing errors. A detailed description of the data processing with SoAP will be provided in a forthcoming publication (Szydlarski et al., in prep.).

---

[1] SoAP is an initiative of the SolarALMA project in Oslo in collaboration with the international solar ALMA development team.
[2] CASA: http://casa.nrao.edu

a) TP Band 3 - SB2, 2016-12-22T14:11:32

b) Radial profiles, uncorrected

c) T_b distribution without correction
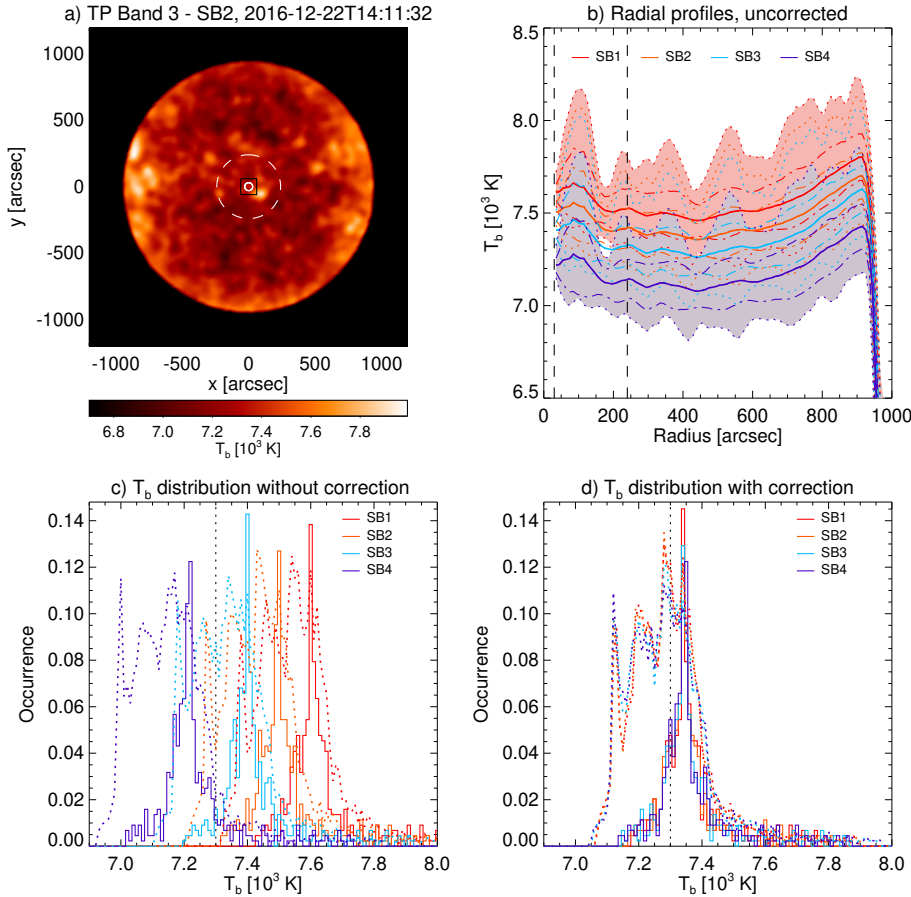
d) T_b distribution with correction

Fig. 1. Brightness temperature distribution in the TP Band 3 maps completed at 2016-12-22T14:11:32. (*a*) Total power map for SB2 (correction following White et al. 2017 applied, i.e. mean value in central region rescaled). The white solid circle in the middle indicates the primary beam of a TP antenna at 3.0 mm and with it the field of view (FOV) of the interferometric observation. The dashed circle has a radius of 240″ and shows the region that is considered for the correction of the absolute brightness temperature scale. The black square shows the central region with 120″ × 120″. (*b*) Uncorrected radial profiles for all sub-bands in rings 10″ in width. The lines for each sub-band (see colour legend at the top) represent the radial average (solid), average plus or minus the standard deviation (dot-dashed), and the 1st and 99th percentile (dotted). The shaded areas cover the value ranges between the percentiles for SB1 (red) and SB4 (blue). *Bottom row*: histograms for the brightness temperature distribution within the black square (solid histograms) and within the white dashed circle (dotted histograms, scaled by a factor of 3) for all sub-bands (*c*) without and (*d*) with correction to the reference value suggested by White et al. (2017) (vertical black dotted line).

2.3. Interferometric field of view

For the Band 3 data discussed here, the full width at half maximum (FWHM) beam width varies from 67.5″ for SB1 to 60.0″ for SB4 with 63.8″ for the band centre frequency (see Appendix A.2 for general background information). As a result of the primary beam taper, the source brightness decreases with distance from the beam axis while the noise stays constant, which means that the signal-to-noise ratio (S/N) declines as function of distance from the beam axis. To correct for the primary beam taper, the image data are divided by the relevant Gaussian (unit maximum) out to some user-specified threshold level where the S/N remains significant. The resulting FOV for interferometric ALMA images is therefore set by the wavelength (or frequency) and the chosen threshold for the primary beam. A threshold of 0.3 is a reasonable but generous choice and results in diameters of the FOV from 89″ (SB1) to 79″ (SB4). In the particular case of the data from December 2016, problems with the pointing and resulting coordinate jumps led to a reduction of the final FOV once the data had been corrected for solar rotation. The resulting FOV of these maps was set to a diameter of 65.6″, which corresponds to effective Gaussian thresholds of 0.52 for SB1 and 0.44 for SB4, respectively.

2.4. Synthesised beam

We define the beam representative for the observations considered here (which determines the angular resolution) as the time-averages of the major axis, minor axis, and position angle. The resulting representative beam corresponds to the band-average frequency of 100 GHz and has a major axis of 2.10″ (FWHM), a minor axis of 1.37″ (FWHM), and a position angle of 68.0 deg.

(see Fig. A.1). The beam for the time step at 2016-12-22 14:42:04 UT comes closest to the representative beam in terms of size. During the 48 min covered during the observation with the Sun moving on the sky, the major axis shrank by ~7% (see Fig. A.1c), whereas the minor axis stayed almost constant and the position angle increased by less than 2 deg (see Fig. A.1d). The changes in the beam must be taken into account for a meaningful interpretation of the resulting data (see Appendix A.3 for more details).

2.5. Absolute temperatures based on total power maps

White et al. (2017) suggest that, until systematic errors in the dual-load calibration scheme are fully understood and resolved, ALMA Band 3 TP maps should be scaled to a prescribed value of 7300 K. The TP maps for the data presented here were produced for each sub-band and calibrated using the dual-load approach described by White et al. (2017) as implemented in CASA[3]. We note that for Band 3 White et al. (2017) recommend using the average over the inner square region with a size 120″ × 120″ (black square in Fig. 1a), whereas the CASA script provided with the TP data uses the average over the central region of the solar disc with a radius of 240″ (40 pixels, see dashed white circle in Fig. 1a). The histograms in Fig. 1c show the absolute brightness temperatures for the two different regions for the different sub-bands. The average brightness temperatures

---

[3] The CASA versions of the dual-load calibration scripts were produced in connection with a meeting of the International Team 387 funded by the International Space Science Institute (ISSI, Bern, Switzerland).
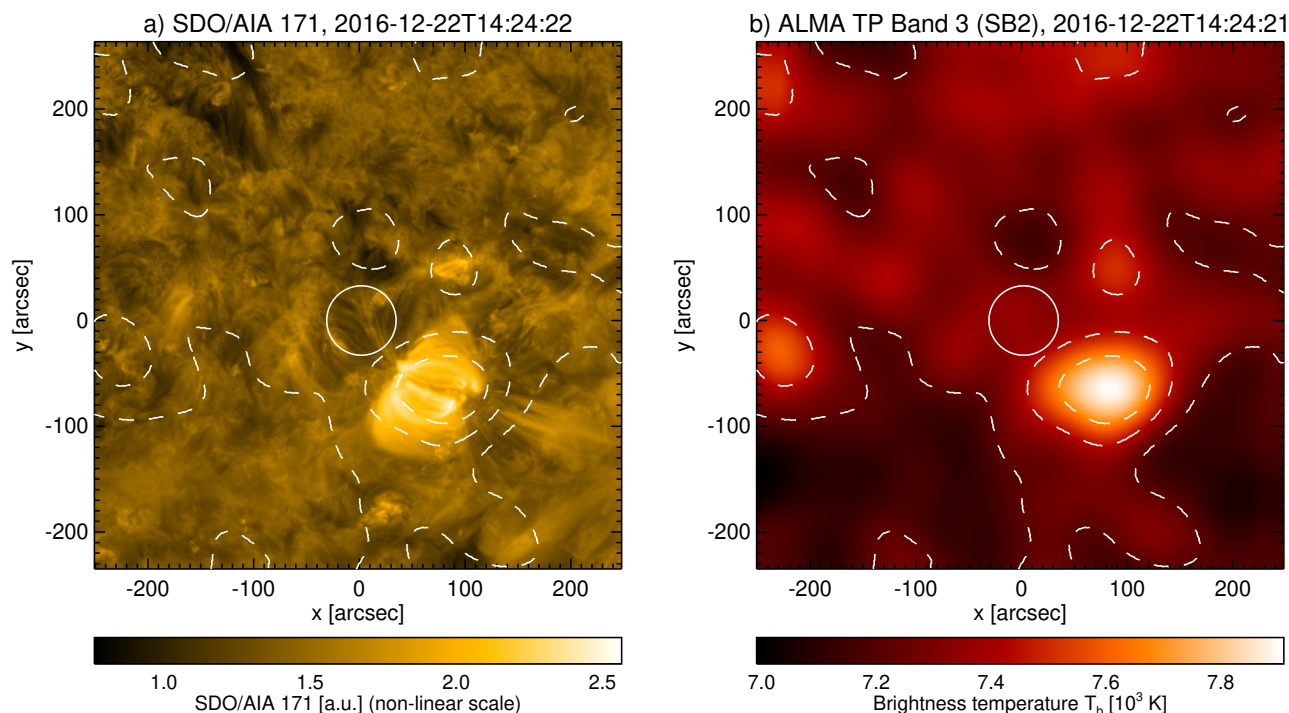
Fig. 2. Context maps for the surroundings of the interferometric field of view (white circle). (*a*) SDO/AIA 17.1 nm. The SDO data are post-processed (level 2) in order to increase the visibility of the atmospheric structure. (*b*) ALMA TP Band 3 (sub-band 2). The white dashed lines are contours for the ALMA data. The displayed data range for the SDO map is limited to 20% of the maximum in order to make dimmer structures more visible. The beam size of the ALMA map is comparable to the shown interferometric FOV.

for the inner $120'' \times 120''$ in the TP map used here (2016-12-22T14:11:32) are 7635 K (SB1), 7529 K (SB2), 7434 K (SB3), and 7247 K (SB4) compared to the corresponding average values for the circular region with radius of $240''$: 7559 K (SB1), 7454 K (SB2), 7357 K (SB3), and 7171 K (SB4). The values for the inner $120'' \times 120''$ region are thus $75-77$ K higher than the larger circular region. It should be noted that the $120'' \times 120''$ region is relatively small considering the width of the primary beam ($\sim 60''$), resulting in poor statistics and susceptibility to untypical brightness temperatures. As a consequence, the histograms for the central square $120'' \times 120''$ in Fig. 1c and d are much narrower than the histograms of the inner region with a radius of $240''$. It should also be noted that the common procedure is to use only one TP sub-band (typically SB2) for determining the offset and in combination with the interferometric data, which thus ignores data from the other three sub-bands.

The above-mentioned mean values, and also the distribution peak temperatures, are highest for SB1 and lowest for SB4, consistent with the expectation that SB1 is formed higher in the solar atmosphere and that the average gas temperature in the mapped layers increases monotonically, for example as reflected by the classic semi-empirical models of Vernazza et al. (1981). On the other hand, the differences between the peak temperatures do not scale according to the sub-band frequencies and are thus not grouped into two pairs, suggesting possible offsets in the brightness temperatures of the order of 100 K. The radial brightness temperature averages in Fig. 1b show the same differences between the sub-bands and thus are of the same order. The standard deviation is for all sub-bands between 100 K and 150 K for radii between $150''$ and $900''$, which is in line with the statistical uncertainty found by White et al. (2017). Following the re-scaling procedure recommended by White et al. (2017) for all interferometric sub-bands separately would then shift the

distributions of all sub-bands to roughly the same peak value (see Fig. 1d). While it does correct offsets between the sub-bands, this procedure would also remove brightness temperature differences between the sub-bands that are connected to slightly different formation heights and the average temperature increase in the chromosphere. The resulting corrected sub-band differences are misleading in the sense that they do not reflect the true temperature gradients in the solar atmosphere.

For the observation presented here we note that there is a bright feature in the inner region (dashed circle in Fig. 1a, see also Fig. 2) that becomes a strong plage or enhanced network region of opposite polarity in the days following the observation. Excluding the bright feature would change the average value for the inner region with radius $240''$ for SB2 from originally 7454 K to 7438 K. This feature alone thus produces a 16 K shift in the absolute brightness temperature scale. Further improvements to the calibration that remove such effects are desirable.

For the data presented here, we strictly follow the procedure implemented in the officially provided CASA script and rescale the average over the (unaltered) central region with a radius of 40 pixels (corresponding to $240''$) in the TP SB2 map to the recommended reference value of 7300 K. The average value in the original SB2 map is 7454 K and thus only 154 K higher than the recommended value, resulting in an applied scaling factor of 0.979 for the whole map. For the moment, significant uncertainties on the TP maps and thus on the absolute brightness temperatures remain, but will be reduced by future improvements in the calibration procedure.

2.6. Final data product and co-observations with SDO

Post-processing with SoAP produced one time series of 1200 full-band (continuum) ALMA maps with a cadence of 2 s
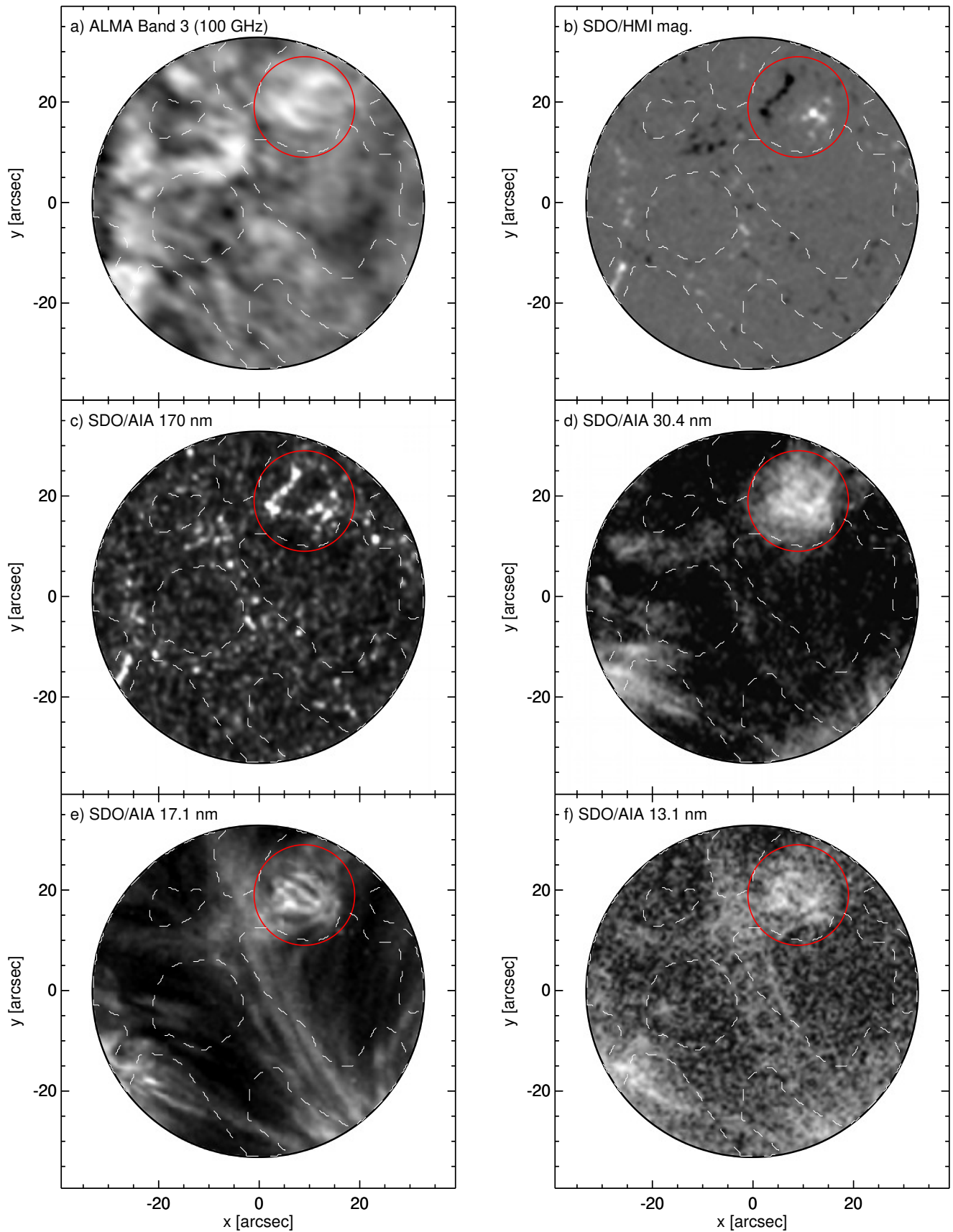
Fig. 3. (*a*) Representative ALMA Band 3 image at 2016-12-22 14:22:52 UT in comparison to co-aligned SDO maps: (*b*) SDO/HMI magnetogram, (*c*) SDO/AIA 170 nm, (*d*) SDO/AIA 30.4 nm, (*e*) SDO/AIA 17.1 nm, (*f*) SDO/AIA 13.1 nm. The SDO data are post-processed (level 2) and re-scaled in order to increase the visibility of the atmospheric structure. The network–internetwork mask is overplotted with dashed contours. The red circle marks a region with a compact group of magnetic loops.
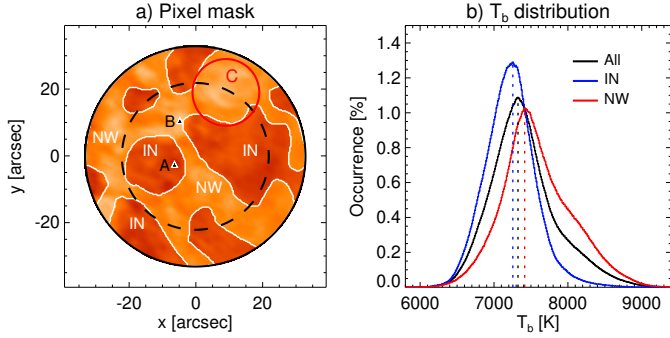
Fig. 4. (*a*) Pixel mask distinguishing between network (NW) and internetwork (IN) pixels (white lines separate NW and IN). The black dashed circle shows the inner region with a radius of 22″. The red circle shows the location of a group of compact loops (labelled C). The triangles show two locations (A and B) for which profiles are shown in Fig. 5. (*b*) Brightness temperature distributions in the inner regions of the FOV (radius $r \leq 22″$) over the whole observing time period. All pixels (black) compared to internetwork (blue) and network pixels (red) for the full band maps.

divided into four scans of ~10 min duration (300 maps each) and intermediate ~2.4 min breaks. As mentioned in Sect. 2.3, the FOV of these maps was limited to a diameter of 65.6″ to ensure that each pixel in the FOV has data for all time steps. The full-disc TP maps for each of the three TP scans are also available for the analysis. Contemporaneous observations with the Solar Dynamics Observatory (SDO; Pesnell et al. 2012) recorded with the Atmospheric Imaging Assembly (AIA; Lemen et al. 2012) and the Helioseismic and Magnetic Imager (HMI; Scherrer et al. 2012) instrument are used here. The ALMA and SDO images have been co-aligned for the whole duration of the observation covering ~47.6 min including ALMA intermediate calibration breaks. A representative time step is presented in Fig. 3a. Movies for the whole time series are available online: (i) The ALMA FOV alone and (ii) in comparison to SDO channels. For the movies, additional boxcar averaging with a window of 20 s is applied (cf. Shine et al. 1994).

2.7. Data mask

The FOV (see Fig. 3a, see also Fig. 2) contains a quiet Sun region with a mixture of magnetic network and internetwork patches. In order to distinguish between quiet Sun internetwork and network pixels, a data mask is constructed based on a combination of time-averaged maps in SDO/AIA 1700 and SDO/AIA 1600 and saturated SDO/HMI magnetograms and the band-averaged ALMA maps. The time-averages include the whole observing period. The final mask is shown in Fig. 4a.

3. Results

3.1. Atmospheric structure observed with ALMA and SDO

An example of full-band maps for ALMA Band 3 is put into context with co-aligned images from SDO in Fig. 3. The statistics for the brightness temperature values for the whole time series are provided in Table 1. The observed quiet Sun region contains a few magnetic network elements that are mostly located in the left and top of the FOV. The network elements appear brighter and thus hotter than their surroundings in the ALMA map (see also the HMI magnetogram in Fig. 3c). A corresponding network mask (which excludes the outermost
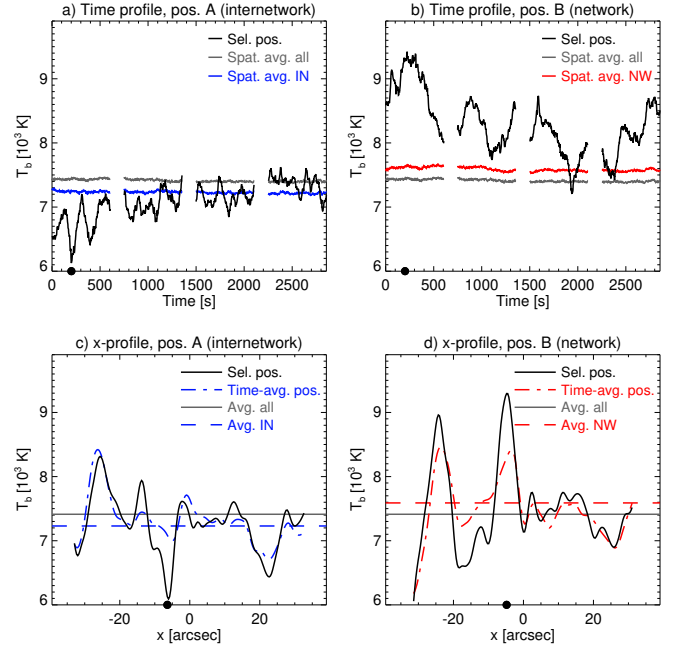

Fig. 5. ALMA brightness temperatures for the two selected positions A (internetwork) and B (network) indicated in Fig. 4. *Upper row*: temporal evolution for (*a*) the internetwork position A and (*b*) the network position B. The dot on the abscissa marks the time step shown in Fig. 3. The temporal evolution of the average over all pixels in the inner region (radius $r \leq 22″$, grey line) and over the contained internetwork (IN, blue line) and network (NW, red line) pixels is plotted for comparison. Profiles along the *x*-axis are shown in the *lower row* for the same time step for (*c*) position A (internetwork) and (*d*) position B (network). The selected spatial position in Fig. 4a is indicated by a dot on the abscissa. For comparison, the time-averages at the selected positions (blue and red dot-dashed lines), the averages over all time steps for all pixels in the inner region (grey solid line) and for the internetwork and network pixels (blue and red dashed lines), respectively, are shown.

Table 1. Observed brightness temperatures in ALMA Band 3 (in Kelvin).

Quantity	All	NW	IN
Avg.	7400	7588	7228
Median	7363	7533	7223
rms	453	478	342
Min.	5814	5828	5814
Max.	9690	9690	9678
1st perc.	6515	6565	6487
99th perc.	8690	8814	8195
Histogram, max.	7325	7415	7254
Histogram, *FWHM*	752	782	702

Notes. Only the inner region of the FOV within a radius of 22″ is considered. Separate values are given for all considered pixels and for the subsets marked as network (NW) and internetwork (IN). Compare Fig. 4a for the pixel map.

part of the FOV) is marked in Fig. 4a. Most of the remaining FOV is characterised by a dynamic mesh-like pattern resembling the pattern seen in other chromospheric diagnostics (e.g., Wöger et al. 2006). The pattern contains dark regions although their temperature differences with respect to the immediate surrounding varies widely. Occasionally, elongated features become discernible temporarily and look like parts of fibrils or dark compact arches, but the visibility of these features varies over
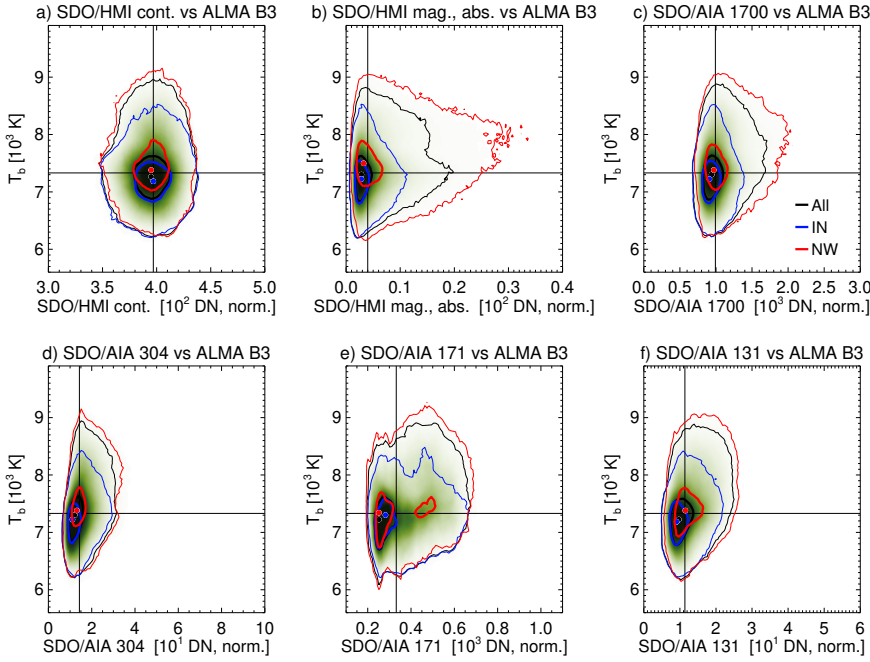
Fig. 6. Correlation of ALMA Band 3 (full-band) with selected SDO channels: (*a*) HMI continuum, (*b*) HMI magnetogram, (*c*) AIA 1700, (*d*) AIA 304, (*e*) AIA 171, and (*f*) AIA 131. All pixels in the inner region of the FOV (excluding the region with the compact loops) for the whole observing period are considered. All SDO maps are convolved with the representative ALMA Band 3 beam. The two-dimensional histograms in each panel are shown in green for all pixels and also with contour levels for all pixels (black), internetwork (blue), and network (red). Thick contours mark levels of 0.5 and thin contours level of 0.01 with respect to the maximum histogram value. The coloured dots show the corresponding maxima. The straight black lines represent the median value for ALMA Band 3 (all pixels) and for the selected SDO channel. We note that the SDO data used here are integration-time-corrected level 1 data numbers (DN) on a linear scale.

time[4]. A comparison of the ALMA maps with the SDO maps suggests that at least some of these features might be connected to extended magnetic loops, as most notably seen in the 17.1 nm map (Figs. 3e and 2a). These features might therefore be caused by weak opacity contributions from coronal loops in the line of sight that then result in weak imprints in the ALMA maps. How significant this effect is should be investigated in the future. The correlation between the ALMA and SDO maps is discussed in Sect. 3.4. The small region marked with a red circle in Fig. 3 is discussed in detail in Sect. 3.5.

3.2. Brightness temperature distribution

Taking into account the whole observation sequence with all 1200 time steps, results in brightness temperatures ranging from ~4440 K to ~10 700 K for all pixels and ~5810 K to ~9690 K in the inner region ($r \leq 22''$). The corresponding average and standard deviation is (7500 ± 514) K for the whole FOV and (7400 ± 453) K for the inner region. The brightness temperature distribution for the whole observing period for the inner region has a maximum at 7325 K (see Fig. 4b). In addition, distributions are shown separately for internetwork and network pixels in Fig. 4b, respectively (see Fig. 4a for the pixel mask). The distribution for network pixels has a peak at a higher temperature compared to the internetwork distribution, and clearly deviates from a Gaussian distribution, exhibiting a stretched tail at higher temperatures. The values for the maxima and widths of the distributions are provided in Table 1. The difference of the distribution maxima for the network pixels and the internetwork pixels is 160 K, whereas the average temperature differs by 360 K. The distributions for the network is about 11% broader than for the internetwork except with a FWHM values of 782 K and 702 K, respectively. These results are compared to other ALMA observations in Sect. 4.1.

3.3. Temporal variation

One position in the internetwork and one in the network are selected and marked in Fig. 4a and labelled A and B, respectively. The temporal evolution of the brightness temperature at these locations is shown in Figs. 5a and b. There seems to be an oscillation with a period of the order of 3 min, as expected for chromospheric internetwork regions, although the variations are more pronounced for other locations in the internetwork. A more detailed study of the oscillatory behaviour will be published in a forthcoming paper (Jafarzadeh et al., in prep.). The network position does not show an equally clear oscillation but variations on different timescales. Brightness temperature profiles along the *x*-axis for the two selected position are shown in Figs. 5c and d, respectively. The major and minor axes (FWHM) of the synthetic beams (see the top of the panels) limit the smallest scales over which variations can be recovered.

3.4. Correlation of ALMA and SDO maps

A comparison of the ALMA maps with the SDO maps reveals that the extended magnetic loops as most notably seen in the 17.1 nm map (Fig. 3e) also leave weak imprints in the ALMA maps. In order to quantify these similarities, the cross-correlations of the ALMA maps with the corresponding SDO maps are calculated for the considered SDO channels. For each time step, the SDO maps are first convolved with the representative ALMA Band 3 beam before calculating the cross-correlation for the whole inner FOV region ($r < 22''$), but excluding the circular region with the compact loops (red circles in Fig. 3). The resulting time-averaged values $\langle C \rangle_t$ are highest for ALMA Band 3 – SDO/AIA 30.4 nm and ALMA Band 3 – SDO/AIA 13.1 nm, both reaching a moderate correlation of $\langle C \rangle_t = 0.38$, followed by SDO/AIA 17.1 nm with $\langle C \rangle_t = 0.33$. The cross-correlation values for only network pixels in the inner region are $\langle C \rangle_t = 0.35$, 0.34, and 0.33 for SDO/AIA 17.1 nm, SDO/AIA 30.4 nm, and SDO/AIA 13.1 nm, respectively. In general, the correlation is much weaker for internetwork pixels with values staying below 0.28 (SDO/AIA 30.4 nm) and
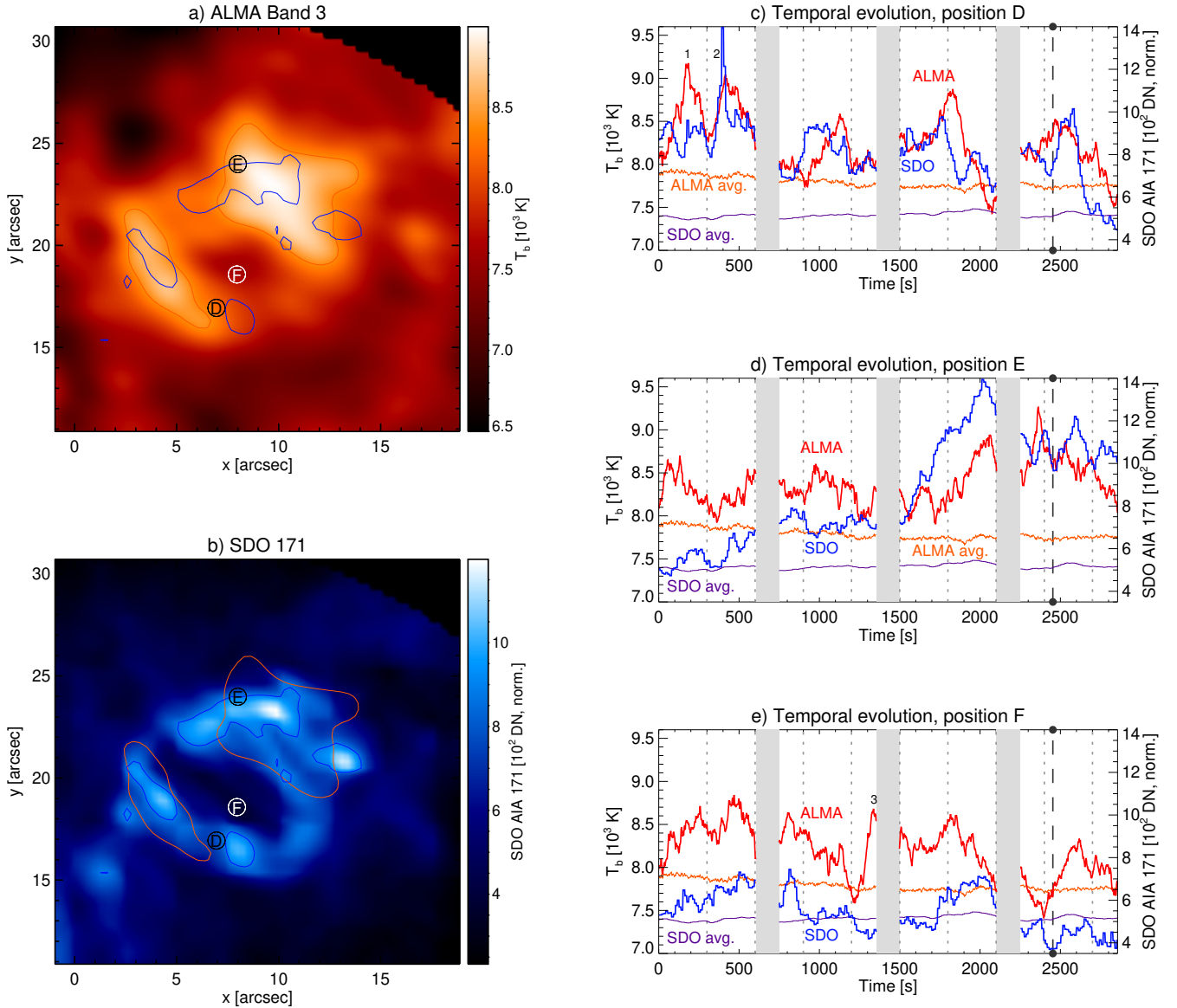
---

[4] The features are more clearly visible in the movies provided as online material.

Fig. 7. Close-up of a group of compact loops (see red circle in Fig. 3). (*a*) ALMA Band 3 brightness temperature map with three selected positions (D, E, F). The red contours indicate a brightness temperature of 8400 K, whereas the blue contours enclose SDO AIA171 values of 880 DN. (*b*) Corresponding SDO AIA171 map with the same contours as in *panel a*. (*c–e*) Time evolution for the Band 3 temperatures (thick red lines) and the SDO 171 values (thick blue lines) for the three selected positions (D: black, E: red, F: blue). Three events showing a temperature increase are labelled 1–3. For comparison, the average over all pixels contained in the close-up region are shown as orange lines for ALMA and purple lines for SDO 171. The calibration breaks with no science data are shown as grey shaded areas. The SDO data used here are integration-time-corrected level 1 data numbers (DN) on a linear scale.

0.19 (SDO/AIA 13.1 nm). The cross-correlation with selected SDO channels is visualised in Fig. 6 for all pixels and also for network and internetwork pixels separately. The plots for SDO/AIA 17.1 nm and SDO/AIA 13.1 nm (panels e and f) reveal the tendency of increasing brightness temperature with increasing SDO count value, implying that statistically a higher value in these channels is connected to a higher brightness temperature along the same line of sight (see Sect. 4.3 for a discussion of potential implications for the formation height ranges of ALMA Band 3).

3.5. Compact loops

In the top right of the interferometric FOV a group of short magnetic loops is visible in most SDO channels (see encircled region

in Figs. 3 and 7b for a close-up). The loops connect patches of opposite polarity, as visible in the HMI magnetogram. Given the appearance in the SDO maps, we suggest that the features in the ALMA maps (see Fig. 7a) are unresolved loop strands. The projected lengths of the loops are of the order of 10″, which agrees with the distance between the magnetic footpoints seen in the HMI map (Fig. 3b). The ALMA map shows higher brightness temperatures at roughly the same location as the hotter SDO channels (panels d–f), implying that ALMA maps the hot loop tops at brightness temperatures between 8500 K and a maximum of 9650 K. Several elongated features with enhanced temperature are discernible. Their widths are 2–3″ and thus close to the resolution limit, whereas the distance of 4–6″ between the elongated features is resolved. Between these features, the brightness temperature can be as low as 7500 K and thus close to the

average value for the whole FOV. The brightness temperature at the loop tops varies strongly in time between approximately 8000 K and peak values of close to or in excess of 9000 K. The temperature difference between the loop tops and the surrounding is thus often of the order of 1000 K or more, although it varies, resulting in varying contrast of the loops. The brightness temperature variations are compared to the corresponding variations in SDO AIA171 for three selected positions (D, E, F) in Figs. 7c–e. At the beginning of the observing period, some loop tops exhibit several consecutive peaks with about 4–5 min in between, which may imply oscillatory behaviour. Positions D and E are located on the loops, whereas position F marks a cooler region between the loops for the shown time step in Fig. 7a. It is quite clear that loops are not properly resolved and also sway in time, thus affecting the signal at a given fixed spatial position. The loop position D shows a strong temperature rise from 8000 K at $t = 20$ s to 9200 K at $t = 170$ s (i.e. 1200 K over 150 s with a corresponding rate of $\sim 8 \, \mathrm{K \, s^{-1}}$) here referred to as event 1. This event is followed by another temperature rise (event 2) with a rate of $\sim 6 \, \mathrm{K \, s^{-1}}$. For event 2, the SDO AIA171 signal also steeply increases at the same time, whereas there is only a moderate increase for event 1. The changes in SDO AIA171 is not always tightly coupled to the changes in ALMA brightness temperature as is most obvious for event 3 at position F. For that event a steep temperature rise of 1100 K over 120 s is observed (i.e. $\sim 9 \, \mathrm{K \, s^{-1}}$), whereas the SDO AIA171 signal slowly decreases.

Analysis of the SDO data for the interferometric FOV and the surroundings (see Fig. 2) before and after the ALMA observation suggests that the compact loop system is the result of a flux emergence event. The first loop top appears in HMI magnetograms around UT9:11 (i.e. about five hours prior to the ALMA observation). Subsequently, two footpoints with opposite magnetic polarity move away from each other and reach their final separation within one hour. In that process, further footpoints emerge next to the initial ones and finally form the group of compact loops. The loops become visible in AIA 171 maps during that emergence phase. After the ALMA observation, the two polarities move towards each other until they mix around UT17:40, followed by the disintegration of the loops. The AIA 304 and AIA 171 data show that the group finally vanishes from about 20 UT.

Such emerging magnetic loops are expected to be optically thin at millimetre wavelengths and may reveal the atmosphere underneath, which could provide the thermal properties of the inner part of emerged regions (Nóbrega-Siverio, priv. comm.). In clear opposition to this expectation, the ALMA observation presented here clearly feature bright magnetic loops, suggesting that they are optically thick and thus block the view of the cool plasma that may be below the loops. A possible explanation is that the observed loop tops are at rather low altitude, at least during the 45 min covered by ALMA. The extended coronal loops that traverse the ALMA FOV (see Fig. 3) seem to be located higher in the atmosphere and might prevent the compact loops from rising higher. The consequence would be that the latter remain in the chromosphere with loops containing plasma with higher density and correspondingly higher opacity.

4. Discussion

4.1. Brightness temperature distribution

The average brightness temperatures in the ALMA Band 3 full-band maps discussed here are of the order of 7400 K for all

pixels in the inner parts of the FOV and of the order of ~ 7590 K and ~ 7230 K when separating network and internetwork pixels (see Table 1). Accordingly, the difference between the average full-band network and internetwork brightness temperatures is ~ 360 K. As expected, these values are close to the reference value of 7300 K suggested by White et al. (2017) because the absolute brightness temperature scale was corrected accordingly. It should be noted, however, that the applied correction was a minor one (see Sect. 2.4). In the following we compare the brightness temperature distributions of the data presented here to the ALMA Band 3 observations from Cycle 4 by Loukitcheva et al. (2019) and Nindos et al. (2018).

Loukitcheva et al. (2019) analyse data obtained on April 27, 2017, for a quiet Sun region at 200″ distance from solar disc-centre that contains magnetic network and internetwork patches. They state a width of 1.6″ for both axes of their synthesised beam, which is slightly smaller than the representative beam used for the data presented here. The brightness temperatures range from 5630 K to 9140 K in their time-averaged map and from 4370 K to 11170 K in the corresponding time sequence at 2 s cadence. The lowest temperatures are found in a 20″ wide region, which is significantly cooler than the surrounding atmosphere, but is not visible at other wavelengths as observed with SDO. From their Fig. 2, we determine the peaks and FWHM values of the brightness temperature distributions for the selected network and internetwork patches. The network patch has a maximum at 7340 K and a FWHM of 1240 K, whereas the internetwork regions have maxima at 7200 K and 7090 K and FWHM values of 530 K and 430 K and corresponding standard deviations of 225 K and 183 K, respectively. In contrast, their cool region has a maximum at 6330 K and a FWHM of 1470 K. The distribution peak temperatures for the internetwork regions are only slightly lower than found in this study (see Table 1 and Sect. 3.2), but it might be argued that they nonetheless agree within the expected uncertainties of possibly a few 100 K. The FWHM of the internetwork temperature distribution found by Loukitcheva et al. (2019) is significantly smaller than for the data set analysed here (702 K, see Table 1). Their distribution for network pixels, on the other hand, has a maximum at 75 K lower than the value found here (see Table 1), but it still agrees within the error limits. The corresponding FWHM, however, is much larger than found in this study. As we demonstrate in Sect. 4.2, the FWHM of the brightness temperature distribution depends on the effective angular resolution of the observation and thus on a number of factors ranging from seeing conditions to details of the image reconstruction procedure.

Nindos et al. (2018) observed the Sun with ALMA in Band 3 on March 16, 2017 for several positions from the limb to disc-centre. For the latter they found an average brightness temperatures of 7530 K for network pixels, 6940 K for internetwork (cell) pixels, and 7220 K for the average over the FOV. We find that the average brightness temperatures for network pixels agree quite well with values for the observations presented here, whereas the value for internetwork pixels found by Nindos et al. (2018) is almost 300 K lower than the value found here. Accordingly, they state an average difference between network and internetwork of 590 K, whereas it is only 360 K in the data presented here (see Table 1). Furthermore, Nindos et al. (2018) determined the standard deviation over the FOV as 390 K compared to ~ 450 K for all pixels in the inner region of the data presented here. The values found by Nindos et al. (2018) is similar to the value found here for internetwork pixels (~ 340–400 K) and lower than the corresponding network value (~ 500 K). Nindos et al. (2018) state that the synthetic beam of their

disc-centre observation has a major axis of 8.1″ and a minor axis of 2.3″, which is significantly larger than the synthetic beams for the data presented here. We note that Nindos et al. (2018) achieved smaller beams for earlier observations closer to the solar limb. The differences in brightness temperatures between those found by Nindos et al. (2018) at solar disc-centre and those reported here might therefore be partially due to the differences in angular resolution in addition to differences arising from the applied post-processing method. We also note that the data run used by Nindos et al. (2018) was obtained under worse seeing conditions with a higher amount of precipitable water vapour (PWV) in the Earth's atmosphere.

For comparison, we considered the BIMA observation by White et al. (2006) at 85 GHz with a beam (and thus an angular resolution) of 10″. White et al. (2006) find rms variations of ~120 K for both network and interwork locations. This value is about a factor 3–4 less than for the ALMA results discussed above.

4.2. Dependence on angular resolution.

As already demonstrated by Wedemeyer-Böhm et al. (2007), not resolving small-scale chromospheric features due to limited angular resolution results in a reduction of the corresponding standard deviation in the obtained brightness temperature maps. The better the angular resolution, the higher the standard deviation in the observations. In the following, we test the influence of reduced angular resolution on the resulting brightness temperature distribution by convolving synthetic brightness temperature maps with different synthetic beams. Brightness temperature maps for ALMA Band 3 frequencies are calculated with the Advanced Radiative Transfer (ART) code (de la Cruz Rodriguez et al., in prep.) for a time series of snapshots from a 3D radiation magnetohydrodynamic simulation with Bifrost (Carlsson et al. 2016; Gudiksen et al. 2011). The series used here has a duration of 20 min and a cadence of 1 s and features an enhanced network region in the middle with surrounding quiet Sun. For each time step the maps for the different frequencies are averaged, resulting in band-average maps (see Fig. 8a for an example of a selected time step). Applying the representative beam for the data presented here (see Sect. 2.4), produces a brightness temperature map at an angular resolution equivalent to the analysed ALMA observations (see Fig. 8b). This procedure is repeated for all maps in the time series and also for the ALMA beams used by Nindos et al. (2018) and Loukitcheva et al. (2019), and the BIMA beam by White et al. (2006). The resulting brightness temperature distributions for the original maps and the degraded maps for all four beams are compared to the observational results in Fig. 8c. All time steps are taken into account. For the elliptic beams such as in the observations presented here and for Nindos et al. (2018), additional degraded maps are calculated with the beam rotated by 90 deg. This extra step reduces possible artificial effects due to the coincidental alignment of elongated features in the original map with a beam axis. The resulting averages and standard deviations of the brightness temperature maps are summarised in Table 2.

The original maps have an average of 7015 K and a standard deviation of 1549 K. The network pixels in the middle of the map (see dashed rectangle in Figs. 8a and b) have an almost 1000 K higher average and a higher standard deviation, whereas both are reduced for the internetwork pixels (outer region of the map in Figs. 8a and b). Reducing the angular resolution by convolution with a synthetic beam (i.e. a PSF) does not affect the brightness temperature average but results in a narrower distribution (see Fig. 8c) and a correspondingly reduced standard deviation
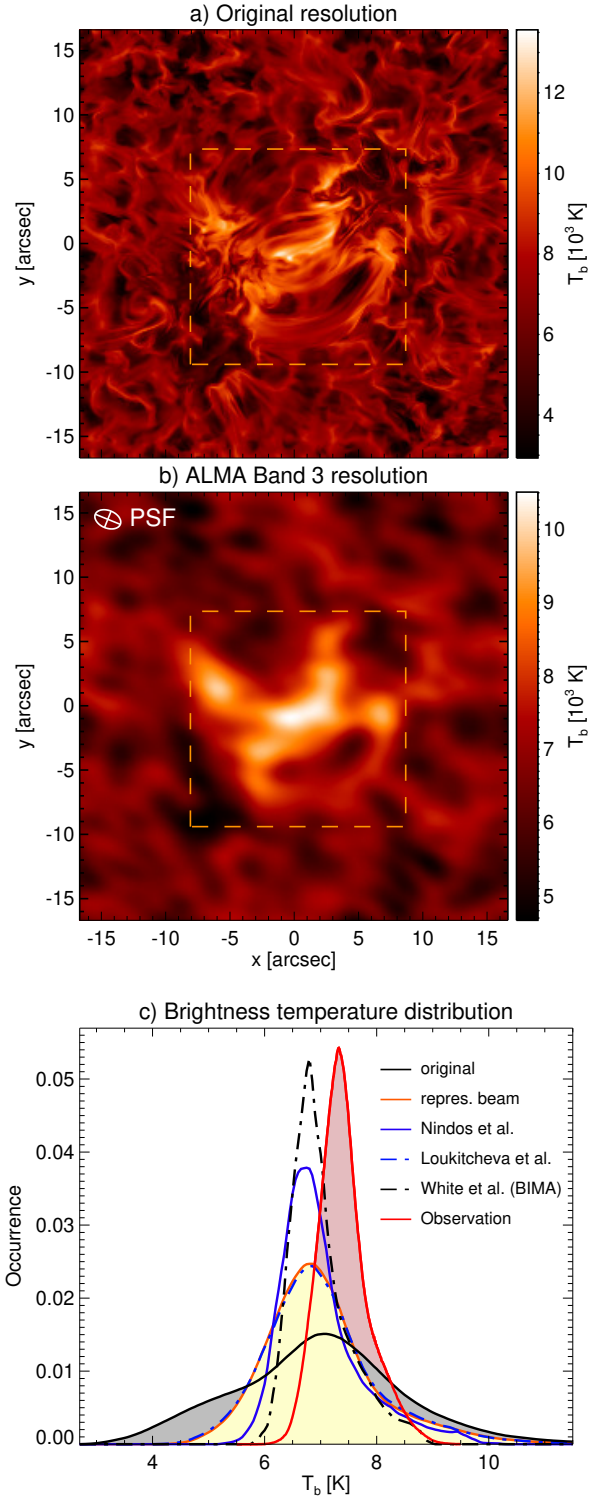
Fig. 8. Selected synthetic brightness temperature map (Bifrost/ART) for the average Band 3 frequency (100 GHz). The enhanced network region is shown with a yellow dashed rectangle. (*a*) The original millimetre map averaged over the frequencies covered by the solar ALMA observations in Band 3. (*b*) The millimetre map after applying the PSF (see upper left corner) corresponding to the representative synthetic beam for the observation presented here. (*c*) The brightness temperature distributions for the original map (black solid line, grey area) and after applying different PSFs: representative beam as in *panel b* (orange solid, yellow area), Nindos et al. (2018; blue solid), Loukitcheva et al. (2019; blue dot-dashed), and White et al. (2006; BIMA, black dot-dashed). The distribution for observed Band 3 temperatures is plotted as a red line and red shaded area (all pixels, see Fig. 4b).

(Table 2). Using the representative beam from the ALMA observations presented here results in a standard deviation of 1033 K, which is very similar to the results obtained with the symmetric 1.6″ wide beam reported by Loukitcheva et al. (2019). The larger and more elliptical beam by Nindos et al. (2018) results in even lower standard deviation of 744 K. For comparison, we also apply the 10″ BIMA beam by White et al. (2006), which returns a standard deviation of 536 K for the whole map and 317 K for internetwork pixels although a substantial mixing of network and internetwork within the beam is expected.

The average brightness temperatures for the whole maps ("All" in Table 2) are only 300 K lower than those derived from the observations presented in this work. The simulated standard deviation, however, is roughly a factor two higher than the corresponding observational value. It is important to note that the original simulated maps represent the best possible maps that can be obtained with a given beam, whereas additional factors can lead to a further reduction of the standard deviation in the observed maps. First of all, interferometric snapshot observations with a finite number of antennas can by nature never provide a truly complete coverage of the spatial Fourier space and resulting degradation must be expected. Furthermore, seeing conditions, noise contributions, and technical details of the imaging process itself are possible causes for further reduction. On the other hand, these first results are already very promising.

We conclude that our results agree with the study by Loukitcheva et al. (2019), at least on a qualitative level, and also in some aspects with Nindos et al. (2018), but more systematic statistical comparisons should be attempted in the future. There are many factors that influence the brightness temperature distribution ranging from the properties of the observed target regions and accuracy of the applied network mask to different seeing condition and details of the imaging procedure. The small size of the FOV and thus the peculiarities of the observed regions will produce variations in the statistical properties derived from different observations. These results should be compared to a corresponding analysis of mosaicking data that cover larger FOVs (see e.g., Bastian et al. 2017; Jafarzadeh et al. 2019). Furthermore, the test for different angular resolutions implies that more extended array configurations of ALMA, which might be offered in future observing cycles, are likely to lead to higher rms variations and thus more contrast in the reconstructed images.

4.3. Formation height

White et al. (2017, and references therein) point out that contributions from the corona to brightness temperatures measured with ALMA should be expected and that the contributions could amount to a few 100 K in Band 3 from the densest parts of the corona. As mentioned in Sect. 3.1 and quantified in terms of cross-correlations in Sect. 3.4, coronal loops that extend across the ALMA field of view and are clearly visible in coronal SDO channels can leave very weak imprints in some ALMA Band 3 maps but are best seen in movies. Internetwork and network regions are clearly seen in the ALMA maps presented here, but appear to be more horizontally expanded than SDO/AIA 170 nm maps, which together with the rather weak to moderate cross-correlation between this SDO channel and ALMA Band 3 may imply that Band 3 is formed above the layer from where the continuum radiation at 170 nm emerges. At the same time, one should be cautious when concluding on the formation height range based on these arguments, especially regarding the cross-correlations, even with these findings supporting the claim by White et al. (2017). Rather, it is essential to study the mapped

Table 2. Simulated brightness temperatures in ALMA Band 3 after applying different synthetic beams in comparison to the ALMA observations.

Quantity	All	NW	IN	Maj	Min	Ang
					Beam	
Original model						
T_b, avg. [K]	7015	7977	6688	–	–	–
T_b, rms [K]	1549	1794	1304			
Convolved with representative ALMA beam, this work.						
T_b, avg. [K]	7015	7969	6691	2.10″	1.37″	68.0°
T_b, rms [K]	1033	1254	693			
Convolved with ALMA beam by Loukitcheva et al. (2019).						
T_b, avg. [K]	7015	7971	6690	1.6″	1.6″	–
T_b, rms [K]	1056	1279	722			
Convolved with ALMA beam by Nindos et al. (2018).						
T_b, avg. [K]	7015	7865	6726	8.1″	2.3″	−48°
T_b, rms [K]	744	802	431			
Convolved with BIMA beam by White et al. (2006).						
T_b, avg. [K]	7016	7681	6790	10.0″	10.0″	–
T_b, rms [K]	536	495	317			
ALMA observations, this work.						
T_b, avg. [K]	7400	7588	7228	2.10″	1.37″	68.0°
T_b, rms [K]	453	478	342			

Notes. The average and standard deviation (rms) are given for all pixels and separately for network (NW) and internetwork (IN) pixels. The major and minor axes (and if applicable the angle) of the applied beam are stated for each case.

height ranges and contribution functions along the line of sight in ALMA data in detail. The scientific potential of the measured brightness temperatures can only be truly unfolded once the temperatures can be assigned to precise height ranges, and can thus be translated into measurements of the chromospheric temperature stratification.

5. Conclusion and outlook

Although the solar observing mode of ALMA is still in its early development phase, the ALMA Band 3 data presented here and in previous publications already demonstrate ALMA's potential for scientific studies of the solar chromosphere. The spatial resolution currently achieved in Band 3 certainly limits the study of the chromospheric small-scale structure and dynamics, but at the same time, and this cannot be emphasised enough, it is an enormous leap forward for the observation of the Sun at millimetre wavelengths.

With this tool at hand, the brightness temperature distribution for a quiet Sun region at disc-centre is quantitatively analysed, also separated in network and internetwork patches, and can thus serve as an important test for numerical simulations of the solar atmosphere.

While many aspects such as the exact formation height ranges, possible weak coronal contributions, and details of the imaging procedure need to be investigated in more detail, the data presented here already allow a wide range of scientific studies. For instance, we are able to measure the brightness temperatures in a group of compact loops as a function of time.

References

Alissandrakis, C. E., Patsourakos, S., Nindos, A., & Bastian, T. S. 2017, A&A, 605, A78
Bastian, T. S. 2002, Astron. Nachr., 323, 271
Bastian, T. S., Ewell, Jr., M. W., & Zirin, H. 1993, ApJ, 415, 364
Bastian, T. S., Chintzoglou, G., De Pontieu, B., et al. 2017, ApJ, 845, L19
Bastian, T. S., Bárta, M., Brajša, R., et al. 2018, The Messenger, 171, 25
Brajša, R., Sudar, D., Benz, A. O., et al. 2018, A&A, 613, A17
Carlsson, M., Hansteen, V. H., Gudiksen, B. V., Leenaarts, J., & De Pontieu, B. 2016, A&A, 585, A4
da Silva Santos, J. M., de la Cruz Rodríguez, J., Leenaarts, J., et al. 2020, A&A, 634, A56
Gudiksen, B. V., Carlsson, M., Hansteen, V. H., et al. 2011, A&A, 531, A154
Jafarzadeh, S., Wedemeyer, S., Szydlarski, M., et al. 2019, A&A, 622, A150
Kundu, M. R., White, S. M., Gopalswamy, N., & Lim, J. 1993, Adv. Space Res., 13, 289
Lemen, J. R., Title, A. M., Akin, D. J., et al. 2012, Sol. Phys., 275, 17
Lindsey, C., Kopp, G., Clark, T. A., & Watt, G. 1995, ApJ, 453, 511
Loukitcheva, M., White, S. M., Solanki, S. K., Fleishman, G. D., & Carlsson, M. 2017, A&A, 601, A43
Loukitcheva, M. A., White, S. M., & Solanki, S. K. 2019, ApJ, 877, L26
Molnar, M. E., Reardon, K. P., Chai, Y., et al. 2019, ApJ, 881, 99
Nindos, A., Alissandrakis, C. E., Bastian, T. S., et al. 2018, A&A, 619, L6
Patsourakos, S., Alissandrakis, C. E., Nindos, A., & Bastian, T. S. 2020, A&A, 634, A86
Pesnell, W. D., Thompson, B. J., & Chamberlin, P. C. 2012, Sol. Phys., 275, 3
Rau, U., & Cornwell, T. J. 2011, A&A, 532, A71
Rodger, A. S., Labrosse, N., Wedemeyer, S., et al. 2019, ApJ, 875, 163
Scherrer, P. H., Schou, J., Bush, R. I., et al. 2012, Sol. Phys., 275, 207
Selhorst, C. L., Simões, P. J. A., Brajša, R., et al. 2019, ApJ, 871, 45
Shimojo, M., Bastian, T. S., Hales, A. S., et al. 2017a, Sol. Phys., 292, 87
Shimojo, M., Hudson, H. S., White, S. M., Bastian, T. S., & Iwai, K. 2017b, ApJ, 841, L5
Shine, R. A., Title, A. M., Tarbell, T. D., et al. 1994, ApJ, 430, 413
Vernazza, J. E., Avrett, E. H., & Loeser, R. 1981, ApJS, 45, 635
Wedemeyer, S. 2016, The Messenger, 163, 15
Wedemeyer-Böhm, S., Ludwig, H. G., Steffen, M., Leenaarts, J., & Freytag, B. 2007, A&A, 471, 977
Wedemeyer, S., Bastian, T., Brajša, R., et al. 2016, Space Sci. Rev., 200, 1
White, S. M., Loukitcheva, M., & Solanki, S. K. 2006, A&A, 456, 697
White, S. M., Iwai, K., Phillips, N. M., et al. 2017, Sol. Phys., 292, 88
Wöger, F., Wedemeyer-Böhm, S., Schmidt, W., & von der Lühe, O. 2006, A&A, 459, L9
Yokoyama, T., Shimojo, M., Okamoto, T. J., & Iijima, H. 2018, ApJ, 863, 96

Appendix A: Introduction to interferometric observations

A.1. Interferometric image reconstruction

Reconstructing solar images from interferometric observations is by its very nature a challenging task that is limited by the achieved sampling of the spatial Fourier domain. Each measurement made by a pair of antennas (a "baseline") with a particular spacing (measured in wavelengths) and orientation corresponds to a single Fourier component[5] of the source brightness distribution. The more Fourier components are measured, the more reliably the original source image can be reconstructed from the available information. For sources that do not change significantly during an observation, the Earth's rotation can be utilised to greatly increase the number of Fourier components measured because the orientation of the antenna distribution relative to the source changes over time. This is referred to as "Earth rotation aperture synthesis". While this technique can be used to better sample the Fourier domain, it is not applicable in the case of variable sources like the Sun. It could be argued that using measurements over short time periods is a justifiable compromise between quality of the reconstructed images and time resolution. The common procedure for the studies published so far (see e.g., Nindos et al. 2018; Loukitcheva et al. 2019) is therefore to reconstruct single images from all available frequency channels from all sub-bands over extended time windows of up to an entire scan (~10 min) or even the full duration of the observations (~1 h). We refer to maps that are constructed from all frequency channels as "full-band" maps, regardless the time window used, whereas the term "snapshot" images is used for maps that are made every integration time. The latter would result in time series of maps with 2 s cadence for Cycle 4 data.

As the Fourier component sampled by a certain baseline also depends on the observing frequency, the sampling in the Fourier domain can be improved by using a wider frequency range for the imaging process, combining spectral channels, and/or all sub-bands. This technique, referred to as frequency synthesis, essentially averages out information in the spectral domain in favour of better image fidelity. Care must be taken in evaluating the trade-offs between improved sampling (and the possibility of improved imaging fidelity) and the loss of information caused by averaging over temporal or spectral variations. Depending on the intended scientific aim, this might not be desirable, and image reconstruction resulting in slightly less reliable brightness temperatures might be acceptable in return for access to the spectral domain. The reliability of brightness temperature differences after splitting into sub-bands is under investigation and will be discussed in greater detail in future publications. For this first paper, we produce maps using all four sub-bands (full-band maps) but we do not average the data in time.

A.2. Interferometric field of view

The FOV of the interferometric observations is set by the primary beam, which is due to the aperture of a single antenna. The

5 The spatial Fourier space is also referred to as "uv space". A component in the uv space is determined by the separation of the two involved antennas (i.e. the baseline length), the observing frequency, and the angles under which the source is observed on the sky.
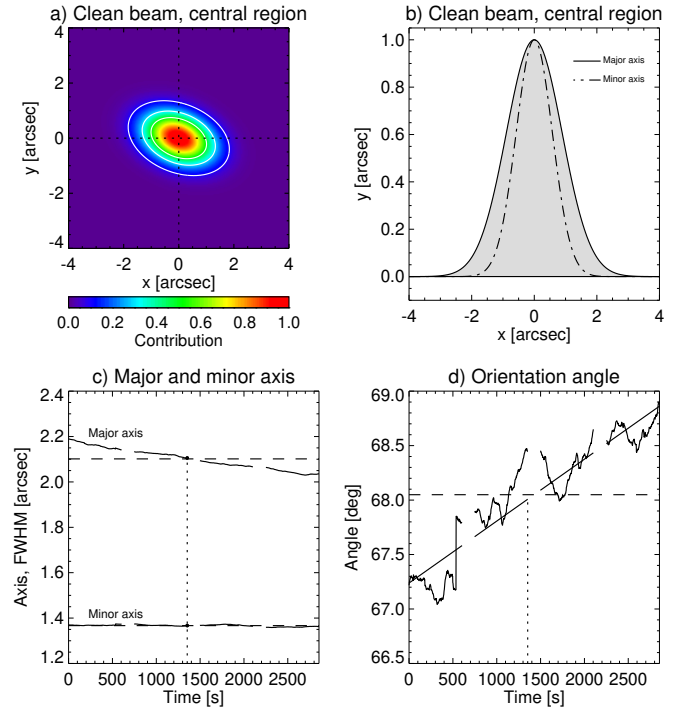
Fig. A.1. Synthesised beam (here also referred to as point spread function, PSF) representative for the Band 3 solar observations. The beam corresponds to the central frequency of 100 GHz. (*a*) Coloured contour plot for the central region around the main lobe, (*b*) profiles along the major and minor axes, (*c*) variation with time for the major and minor axes, and (*d*) for the orientation angle. The dashed horizontal lines in the *lower panels* mark the time-averages of the beam parameters, while the dotted vertical lines mark the time of the actual full-band beam that is closest in size to the representative beam as derived from the time-average of the major and minor axes.

effect of the primary beam response is to multiply the field of view by an approximately Gaussian function, referred to as the primary beam taper. The size of the Gaussian primary beam is typically specified in terms of its FWHM, which depends on the observed wavelength (or frequency; see e.g., Wedemeyer et al. 2016).

A.3. Synthesised beam

The synthesised (interferometric) beam, which corresponds to the point spread function (PSF) of the interferometric array, is calculated during the image reconstruction process and provided as output. The PSF depends on the angles under which the target appears on the sky, and thus changes with time when the target is tracked during an observation. The ALMA PSF is characterised by a central lobe normalised to unit amplitude and side lobes due to incomplete sampling in the Fourier domain. The central lobe is approximately an elliptical Gaussian, whose dimensions are determined by the maximum distances between antennas, thus determining the angular resolution of the observation. Image deconvolution involves removal of the PSF side lobe response from the image leaving, in principle, a map that is the true brightness distribution convolved with the "clean beam" plus noise. In general, the clean beam is simply the elliptical Gaussian fit to the central lobe of the PSF (Fig. A.1a).

A.4. Absolute temperatures based on total power maps

The interferometric observations provide brightness temperature differences relative to the mean brightness, but lack an absolute offset corresponding to the measurement at the zero spatial frequency (or zero-spacing frequency) in the Fourier domain. That is, the zero component corresponds to a telescope pair with a baseline of zero length. Since this is technically impossible, ALMA overcomes this problem by combining interferometric data with observations with single-dish total power antennas. These antennas have a diameter of 12 m like the other antennas in the ALMA 12 m array. The angular resolution of the full-disc maps produced by TP fast-scanning techniques is therefore identical to the FOV of the 12 m array. While details on spatial scales below ≈60″ remain unresolved in TP maps, the features in the map can clearly be correlated with full-disc maps obtained with the Solar Dynamics Observatory (SDO; Pesnell et al. 2012) (see Sect. 2.6). We note that a single measurement with a TP antenna toward the interferometric target provides the zero-spacing component in Fourier space, whereas fast-scanning over the solar disc measures the brightness distribution of the source on angular scales of the primary beam (here ~60″) and larger (to the angular extent of the Sun itself).